



Model-free Maps of Interstellar Neutral Hydrogen Measured with *IBEX* between 2009 and 2018

A. Galli¹ , P. Wurz¹ , F. Rahmanifard² , E. Möbius², N. A. Schwadron² , H. Kucharek², D. Heitzler², K. Fairchild², M. Bzowski³ , M. A. Kubiak³, I. Kowalska-Leszczynska³ , J. M. Sokół³ , S. A. Fuselier⁴, P. Swaczyna⁵ , and D. J. McComas⁵

¹ Physics Institute, University of Bern, Bern, 3012, Switzerland

² University of New Hampshire, Durham, NH 03824, USA

³ Space Research Centre, Polish Academy of Sciences, Warsaw, 00-716, Poland

⁴ Southwest Research Institute and University of Texas, San Antonio, TX 78228, USA

⁵ Department of Astrophysical Sciences, Princeton University, Princeton, NJ 08544, USA

Received 2018 October 8; revised 2018 December 7; accepted 2018 December 7; published 2019 January 22

Abstract

The *Interstellar Boundary Explorer* (*IBEX*) is a NASA satellite in Earth orbit, dedicated to observing interstellar neutral (ISN) atoms entering the heliosphere and energetic neutral atoms from the heliosheath from 11 eV to 6 keV. This work presents comprehensive maps of ISN hydrogen observed with *IBEX* at energies between 11 and 41 eV, covering almost an entire solar cycle from 2009 to 2018. ISN hydrogen measurements can provide information on the interstellar medium and on the heliosphere that modifies the incoming ISN flow. Whereas hydrogen is the dominant species in the unperturbed interstellar medium, most ISN hydrogen atoms crossing into the heliosphere do not reach the inner solar system: some are filtered out around the heliopause, while others are held off by solar radiation pressure or may be ionized as they approach the Sun. This paper presents and evaluates several approaches for generating model-free maps of ISN hydrogen from *IBEX* measurements. We discuss the basic implications of our results for ISN hydrogen inflow and outline the remaining discrepancies between observations and model predictions. Our maps show, during weak solar activity from 2009 to 2011, a clear signal of ISN hydrogen for ecliptic longitudes between 240° and 310°, roughly one month after the signal of ISN helium has peaked. When the solar activity approached its maximum around 2014, the ISN hydrogen signal weakened and dropped below the detection threshold because of increasing solar radiation pressure and ionization. The ISN hydrogen signal then reappeared in 2017.

Key words: ISM: atoms – plasmas – solar wind – Sun: heliosphere

1. Introduction

The *Interstellar Boundary Explorer* (*IBEX*) has been continually observing the interaction of the heliosphere with the surrounding interstellar medium since 2009 January (McComas et al. 2009a). *IBEX* orbits the Earth at distances between 48,000 and 320,000 km, measuring neutral atoms from the heliosphere and from the interstellar medium at energies from 11 eV to 6 keV. The scientific payload consists of two instruments, *IBEX*-Lo (Fuselier et al. 2009) and *IBEX*-Hi (Funsten et al. 2009). The first studies on interstellar neutral hydrogen (ISN H) observed with *IBEX*-Lo from 2009 to 2012 were published by Saul et al. (2012, 2013) and Schwadron et al. (2013). Because ISN H traveling toward the inner heliosphere is strongly affected by solar radiation and solar wind, we have refocused our attention on ISN H as the second solar minimum during *IBEX* observations is expected for 2019–2020. We have collected all available *IBEX* observations of ISN H measured between 11 and 41 eV from 2009 to 2018, expanding previous studies in terms of spatial and temporal coverage and also in terms of retrieval methods.

Similar to the study of ISN helium and oxygen (see, for instance, the recent contributions by Kubiak et al. 2016; Park et al. 2016; Bzowski et al. 2017), ISN H data provide information on the interstellar material and on the heliosphere that modifies the incoming ISN flow. The main challenge with ISN H measured at 1 au is how to discern the signal from the background and from the intense signal caused by ISN helium:

hydrogen is the dominant species in the unperturbed interstellar medium (Gloeckler & Geiss 2001; Müller & Zank 2004), but most ISN atoms that make it to the inner solar system without being reionized are helium. In addition, a portion of ISN helium reaches Earth’s orbit as a spatially extended secondary component with lower energies (Kubiak et al. 2014). Helium atoms can generate hydrogen and oxygen counts in the *IBEX*-Lo instrument by sputtering off the water layers on the conversion surface (Möbius et al. 2012), whereas ISN H generates mostly hydrogen counts. A proper identification of ISN H therefore benefits the study of both ISN H and helium.

Figure 1 shows a sketch of ISN H and He flowing toward *IBEX* orbiting the Sun. The numbers in black denote *IBEX* orbit numbers specific to the first ISN season from 2009 January to April, and the red arrows indicate the flow direction of ISN H into the heliosphere: solar radiation pressure is comparable to the Sun’s gravitational force for H trajectories (Schwadron et al. 2013; Kowalska-Leszczynska et al. 2018a, 2018b), whereas it is negligible for He. Moreover, charge exchange with the solar wind has a much higher probability for H than for He atoms. The ISN H signal therefore is expected to move toward larger ecliptic longitudes (later *IBEX* orbits) and to become weaker during high solar activity.

Based on the first four years of *IBEX* data, which started at the previous solar minimum in 2008 December (SILSO, World Data Center 2008), the *IBEX* team reported the first direct detection of ISN H in the solar system: in 2009 March and April, in the two lowest energy bins of *IBEX*-Lo centered

Table 1
Overview of the Data Set: 10 years of ISN Seasons. From 2011 October Onwards, the Orbits are Evaluated in Two Separate Half Arcs

Period	PAC Voltage	Energy Steps	Orbits Included
2008 Dec–2009 Jun	Nominal	1-2-3-4-5-6-7-8	11–31
2009 Oct–2010 Jun	Nominal	1-2-3-4-5-6-7-8	49–80 (without 62)
2010 Nov–2011 Jun	Nominal	1-2-3-4-5-6-7-8	102–127 (without 110–114)
2011 Nov–2012 Jun	Nominal	1-2-3-4-5-6-7-8	145a–169b (without 150b–156a)
2012 Oct–2013 Jun	Lowered	1-2-3-4-5-6-7-8	183a–209b (without 207)
2013 Oct–2014 Jun	Lowered	1-2-3-4-5-6-7-8	223a–249b
2014 Oct–2015 Jun	Lowered	1-2-3-4-5-6-7-8	262a–288b
2015 Oct–2016 Jun	Lowered	1-1-2-2-5-6-7-8	305a–328b (without 316)
2016 Sep–2017 May	Lowered	1-1-2-2-3-6-7-8	340a–367b
2017 Sep–2018 May	Lowered	1-1-2-2-3-6-7-8	381a–407b (without 390 and 405)

measurements are combined to verify that the count was due to a true H^- or O^- ion entering the TOF unit at the expected speed given the known mass. This excludes many counts caused by electrons or UV photons and greatly enhances the signal-to-noise ratio (Möbius et al. 2008). For nominal energy stepping, there are 2×8 data blocks of triple coincidence counts of H^- and O^- in the eight energy steps for each 15 minute segment.

The observation times for this study include all available *IBEX*-Lo triple coincidence data of hydrogen ENAs, yielding annual maps of ISN H from 2009 to 2018. The year 2016 had to be excluded from most analyses because *IBEX*-Lo was run in a non-nominal energy stepping mode during the orbits when the ISN signal peaked: the integration times for energy bins 1 and 2 were doubled at the expense of measurements in energy bins 3 and 4. Table 1 lists the years and orbits included in the study, adding the energy stepping pattern during the ISN season and the post-acceleration voltage (PAC) settings. After 2012, the lowered PAC led to a lowered sensitivity for oxygen and other atoms heavier than helium. The resulting O^- maps therefore can no longer be used to discern ISN He from ISN H. The data set includes only the times with the lowest background levels; measurements affected by high electron background were excluded using the method described by Galli et al. (2016).

As an example, Figure 2 shows the maps of raw H^- count rates measured in energy bin 1 during the 2018 season in two different map formats. The bottom panel shows orbit versus spin whereas the upper half (spin angles of 180° – 360°) corresponds to signals from the ram, and the lower half from the anti-ram, direction. Each orbit is subdivided into two half arcs. The top panel of the plot shows the ram hemisphere data rebinned into $6^\circ \times 6^\circ$ pixels of ecliptic longitude versus latitude. The peak intensity around 225° is the primary ISN helium component; the extended tail earlier in the season is the secondary helium population, also called the Warm Breeze (Kubiak et al. 2014, 2016); and the faint tail around $\lambda_{\text{ecl}} = 270^\circ$ after the ISN He maximum is due to ISN H. The row of high count rates at spin angle = 20° in the upper panel is an artifact of the data acquisition. This artifact is easily excluded from further analysis as it appears at a spin angle far away from the ISN signal. Note that pixels with an intensity or count rate above the upper limit of the color bar scale are colored red in all maps throughout the paper. The raw H^- and O^- count rate maps in the orbit versus spin angle format (bottom panel of Figure 2) served as the input from which we derived ISN hydrogen intensities. The methods to derive these intensities are explained in the following section.

3. Retrieval Methods for ISN Hydrogen

The maps of the raw count rates were first cleaned of all signals other than ISN H and ISN He: magnetospheric contamination, heavy ISN species, heliospheric ENAs, and instrument background. We then used several approaches to derive the ISN H intensities from the remaining H^- and O^- count rates.

3.1. Subtraction of Known Background Sources

ISN oxygen and neon enter *IBEX*-Lo at energies of typically 100–200 eV and are routinely observed in energy bins 5 and 6 (Park et al. 2016). These heavy species produce a few H^- and O^- counts at lower energies in bins 1 to 4, but this contribution is negligible compared to ISN He and H according to laboratory calibration: the sputtered O^- in energy bins 1 and 2 caused by ISN Ne and O is less than 0.3% of the measured O^- count rates due to ISN He at the position of the ISN He peak. Likewise, the sputtered H^- caused by ISN Ne and O is less than 0.5% compared to the H^- count rates due to ISN H.

Magnetospheric contamination appears as erratic bright pixels early in the ISN season (September–November) when *IBEX* is close to Earth’s bow shock for most of the orbit. Because it represents a highly time-variable physical signal, magnetospheric contamination is not easily modeled. We excluded individual affected pixels by defining a mask in the H^- maps of energy bin 5 (where no ISN signal is seen) and assuming that a pixel was contaminated if its count rate was 3.5 times higher than the median of all pixels for that season with non-zero count rates. Such contaminated pixels were then excluded from further analysis, showing up as white pixels in the maps of the derived ISN H. Lower levels of magnetospheric ENA emissions may be left in the data and represent a residual background.

The remaining non-ISN background sources (heliospheric ENAs and background related to the magnetosphere or the instrument) were subtracted from the raw count rate before further evaluation. This background level was derived as follows: for each energy bin, orbit, and species (H^- or O^-), the average count rate observed from the anti-ram hemisphere was calculated and used as an estimate for the sum of backgrounds not due to ISN and subtracted from the pixels in the ram hemisphere. This procedure is based on the knowledge that *IBEX*-Lo cannot detect any ISN signal above the background from anti-ram directions (Galli et al. 2015). Averaged over a season, these background estimates are consistent with the ubiquitous background count rates derived for the years 2009–2016 (Galli et al. 2015, 2017). This is illustrated in

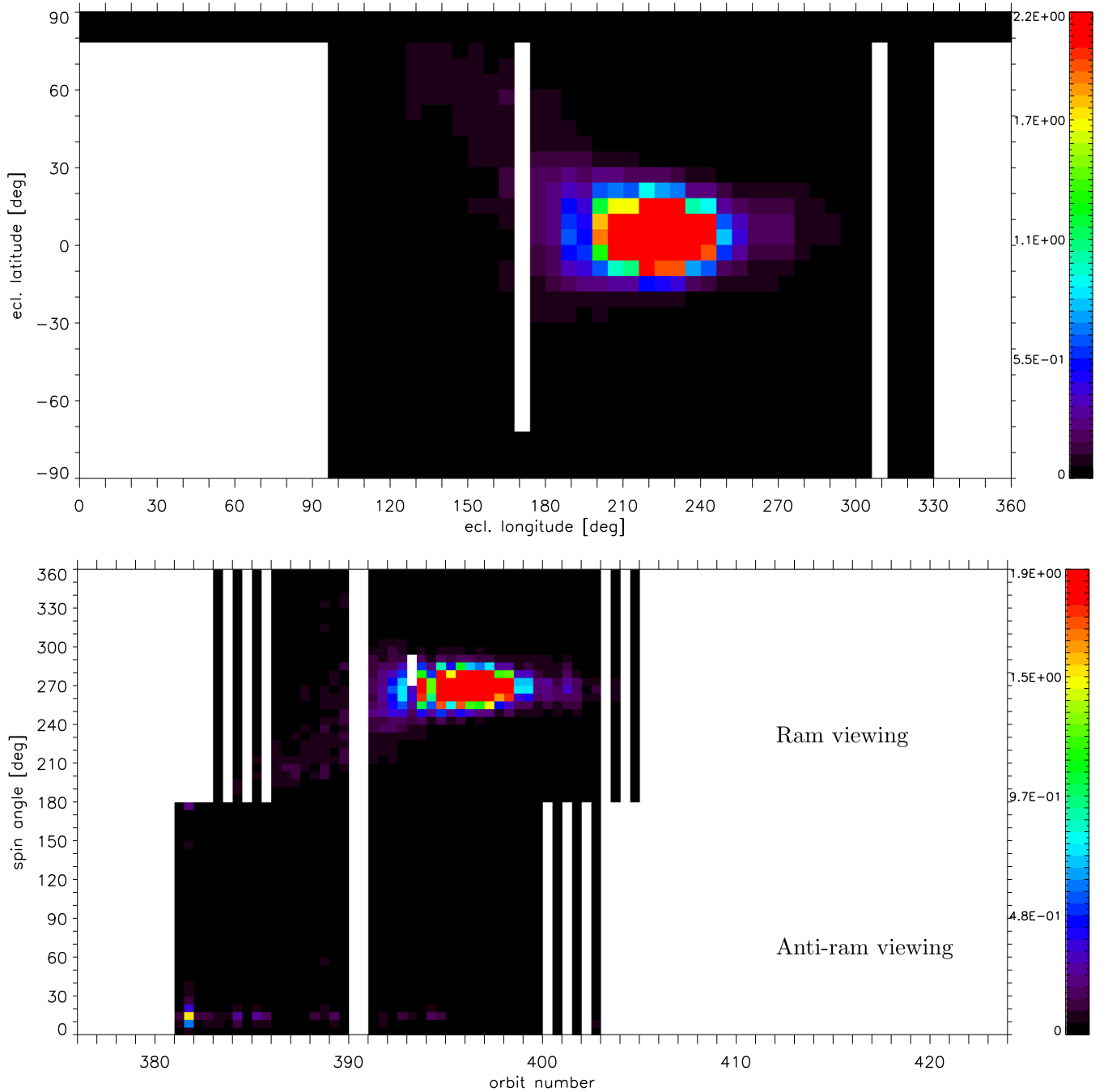


Figure 2. Example maps of raw H^- count rates measured in energy bin 1 during the 2018 season. Bottom: orbit number vs. spin angle format, top: ram measurements rebinned into a rectangular $6^\circ \times 6^\circ$ grid of ecliptic coordinates. Pixels whose intensity or count rates exceed the upper limit of the color scale (stated on the bar) are colored red in these and all other maps.

Figure 3: the symbols indicate the average empirical background subtracted in this study in the three lower energy bins before and after the PAC change; the solid and dashed lines indicate the ubiquitous background levels and their uncertainties (Galli et al. 2015, 2017). Like the ubiquitous background, our empirical estimates are constant with time except for the instrument-related drop in summer 2012 when the PAC had to be reduced. If a fraction of the empirical background is due to heliospheric ENAs, this does not affect the derived ISN intensities in the ram hemisphere: the heliospheric ENA signal rolls over or follows a power law with a spectral index γ not

steeper than -1 at energies of 10 to 100 eV for any viewing direction (Galli et al. 2017; Zirnstein et al. 2018). If the heliospheric ENA signal rolls over, it does not contribute to the total count rate at ISN H energies (below 40 eV). If it follows a power law with $\gamma = -1$, then the corresponding count rates below 40 eV do not vary with ecliptic latitude and are therefore properly subtracted from the total of the measured count rates.

For error analysis, the uncertainty of the remaining H^- or O^- count rate C was assumed to be

$$\sigma_C = \sqrt{\sigma_{bg}^2 + (C + C_b)\xi}, \quad (1)$$

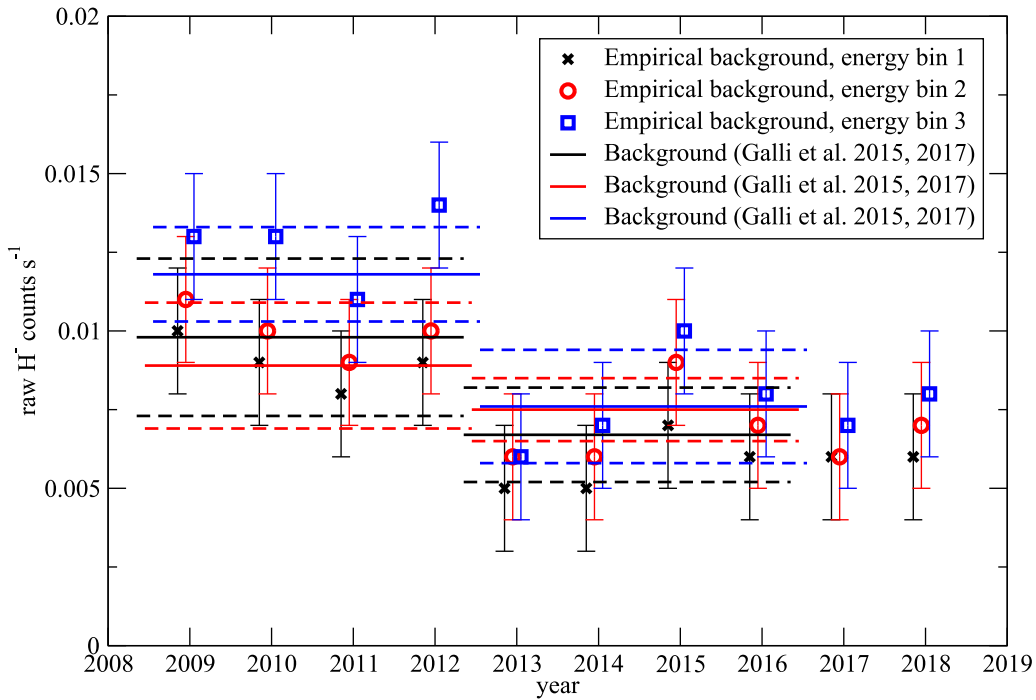


Figure 3. Time series of background rates averaged over the entire season for anti-ram hemisphere observations (symbols) compared with the ubiquitous background (solid lines: most likely values, dashed lines: 1σ uncertainties) derived by Galli et al. (2015, 2017) for the region between 300° and 360° ecliptic longitude for ram and anti-ram observations.

with $\sigma_{bg} = 0.002$ or 0.001 cts s^{-1} for H^- and O^- , respectively, being the uncertainty of the subtracted background, C_b the count rates due to background, and $\xi = 0.003$ cts s^{-1} the one count per orbit limit (which is needed to calculate the statistical uncertainty due to Poisson statistics). The resulting uncertainty of the reduced count rate is included in the final error analysis, but it has a minor impact on the derived ISN H intensities. If, for instance, the constant background rates (Galli et al. 2015, 2017) instead of the empirical background rates C_b are subtracted, the derived ISN H intensities j in energy bin 1 change at most by a few percent for any $j \geq 10^4$ $cm^{-2} sr^{-1} s^{-1}$.

3.2. Conversion of Count Rates into ISN H Intensities

We studied different methods for converting count rates into ISN H intensities. The goal of all approaches was to differentiate the H^- counts caused by ISN H from those caused by the intense ISN He signal. This is achieved thanks to the different energies of the two species: ISN H reaches *IBEX*-Lo with a relative energy <40 eV at any time or viewing direction (based on the WTPM predictions). Thus, ISN H can only create a detectable H^- signal in energy bins 1 (11–21 eV) and 2 (20–41 eV), whereas ISN He, with relative energy inside energy bin 4 (78–155 eV, Swaczyna et al. 2018), causes a H^- and O^- signal via sputtering in all energy bins from 4 down to 1 (Möbius et al. 2012). Exploiting these distinctions, we found three useful methods for deriving maps of ISN H:

1. H3_inflight: Based on H^- maps in energy bins 1 to 3 and inflight calibration of the He response.
2. H3_lab: Based on H^- maps in energy bins 1 to 3 and laboratory calibration of the He response.

3. H2O2_inflight: Based on H^- and O^- maps in energy bins 1 and 2 and inflight calibration of the He response.

The approaches H3_inflight and H3_lab rely on a bootstrap method. We first calculated the He intensity at a map pixel ($J_{He}(i, j)$) from the H^- count rate in energy bin 3 ($C_{3H^-}(i, j)$, covering 39–77 eV); ISN H with its energy below 40 eV is expected to contribute nothing to this count rate. Knowing the ISN He intensity, we then calculated the H^- count rates in energy bin 2 caused by ISN He. If more H^- count rates were registered than expected, we attributed this excess to an ISN H intensity of energies 20–41 eV ($J_{H,2}(i, j)$). We repeated this approach for energy bin 1 to derive $J_{H,1}(i, j)$ at 11–21 eV. Mathematically,

$$\begin{aligned}
 \text{I) } J_{He}(i, j) &= C_{3H^-}(i, j) / g_{3He \rightarrow H^-}(i, j) \\
 \text{II) } J_{H,2}(i, j) &= (C_{2H^-}(i, j) \\
 &\quad - J_{He}(i, j) g_{2He \rightarrow H^-}(i, j)) / g_{2H \rightarrow H^-} \\
 \text{III) } J_{H,1}(i, j) &= (C_{1H^-}(i, j) - J_{He}(i, j) g_{1He \rightarrow H^-}(i, j) \\
 &\quad - J_{H,2}(i, j) g_{2H \rightarrow H^-}(i, j)) / g_{1H \rightarrow H^-}. \quad (2)
 \end{aligned}$$

The conversion factors like $g_{1He \rightarrow H^-}$ describe how many H^- counts are produced in a given energy bin by an incoming He or H atom. Because the instrument sensitivity usually depends on the energy of the incoming He atom, and the energy of He changes with longitude and latitude, the conversion factor generally varies for different map pixels (i, j). Provided that there is no unidentified background left in the data, the reliability of the derived ISN H and ISN He intensity depends solely on the knowledge of these conversion factors.

For the H3_lab approach, we used the $g_{He \rightarrow H^-}$ from the laboratory calibration (Table 9 in Park et al. 2016). Those are averages over the range of a given energy bin and therefore do not vary with energy or viewing direction. These simplified

Table 2

Energy-independent Conversion Factors between Neutral He and H Intensities and Measured H^- Count Rates in Energy Bins 1, 2, and 3 (Park et al. 2016)

	Conversion factor [$\text{cm}^2 \text{sr}$ eV/eV] before the PAC change (2009–2012)	Conversion factor [$\text{cm}^2 \text{sr}$ eV/eV] after the PAC change (after summer 2012)
$g1_{\text{He} \rightarrow \text{H}^-}$	$0.93 \times 4.89 \times 10^{-5}$	$0.434 \times 4.89 \times 10^{-5}$
$g2_{\text{He} \rightarrow \text{H}^-}$	$0.93 \times 6.03 \times 10^{-5}$	$0.435 \times 6.03 \times 10^{-5}$
$g3_{\text{He} \rightarrow \text{H}^-}$	$0.88 \times 5.22 \times 10^{-5}$	$0.437 \times 5.22 \times 10^{-5}$
$g22_{\text{H} \rightarrow \text{H}^-}$	$0.93 \times 1.41 \times 10^{-5}$	$0.435 \times 1.41 \times 10^{-5}$
$g21_{\text{H} \rightarrow \text{H}^-}$	$0.93 \times 4.23 \times 10^{-6}$	$0.434 \times 4.23 \times 10^{-6}$
$g11_{\text{H} \rightarrow \text{H}^-}$	$0.93 \times 7.29 \times 10^{-6}$	$0.434 \times 7.29 \times 10^{-6}$

Note. By default, the absolute uncertainties of all these factors are assumed to be 30% (Fuselier et al. 2009).

conversion factors are stated in Table 2. The PAC change in 2012 decreased the instrument sensitivity and thus changed the conversion factors. Table 2 also lists the conversion factors for neutral H with energy corresponding to the range 11–21 and 20–41 eV leading to H^- count rates. The uncertainty of all these conversion factors from laboratory calibration was assumed to be 30% (Fuselier et al. 2009). For a complete list of all laboratory calibration values for H, He, and heavy neutrals, the reader is referred to Table 9 in Park et al. (2016).

For the H3_inflight approach, we plotted the instrument count rates during the orbits where the primary ISN He signal peaked (orbit 396 or $\lambda_{\text{ecl}} = 225^\circ$ in Figure 2) versus He energy. For these orbits, the ISN He signal is orders of magnitude stronger than any other signal (including ISN H). We used the $C1_{\text{H}^-}(i, j)$ maps at these orbits as input, presumed the $g1_{\text{He} \rightarrow \text{H}^-}$ from the laboratory calibration, and derived the conversion factors $g2_{\text{He} \rightarrow \text{H}^-}$ and $g3_{\text{He} \rightarrow \text{H}^-}$ from the H^- signal in energy bins 2 and 3 as a function of the modeled helium energy for the full energy range from 30 to 135 eV. The He energy was calculated as the flux-weighted mean of the energies of the primary and the Warm Breeze component, for which we assumed the model parameters from Swaczyna et al. (2018; row 10 in Table 2) for the primary He component and Kubiak et al. (2016) for the Warm Breeze He component.

Figure 4 presents, as two examples, the fits and the raw data used to derive the conversion factors $g2_{\text{He} \rightarrow \text{H}^-}$ before the PAC change and $g3_{\text{He} \rightarrow \text{H}^-}$ after the PAC change. The fits are unweighted linear regressions or arithmetic means (red solid lines in Figure 4); the uncertainties are chosen in such a way that 68% of all data points fall within the average plus/minus the uncertainty (red dashed lines). The uncertainty of the inflight conversion factors depends on the scatter around the fit functions, varying between 4% and 30%. The year-by-year variability of the conversion factors turned out to be negligible compared to this uncertainty; only the factors derived before and after PAC change had to be differentiated. Below a certain cutoff, the ISN He energy becomes too low to create H^- counts in energy bin 3. This cutoff energy increased from 65 ± 5 eV to 75 ± 5 eV (blue dashed-dotted line in lower panel of Figure 4) when the PAC changed in 2012. Because the ISN energy decreases with higher latitude (Swaczyna et al. 2018), the H3_inflight approaches relying on H^- counts in energy bin 3 cannot be applied to derive ISN H in energy bins 1 and 2 for ecliptic latitudes beyond $\pm 54^\circ$ for 2009–2012 or beyond $\pm 48^\circ$

after 2012. The corresponding latitudes or spin angles in the ISN H maps were therefore blanked out. In the lower energy bin 2, the instrument registered H^- counts even for ISN He energies as low as 40 eV (top panel of Figure 4).

For the H2O2_inflight approach, the bootstrap method, in analogy to Equation (2), is

$$\begin{aligned} \text{I) } J_{\text{H},2}(i, j) &= (C2_{\text{H}^-}(i, j) \\ &\quad - r_2(i, j) C2_{\text{O}^-}(i, j)) / g22_{\text{H}^- \rightarrow \text{H}^-} \\ \text{II) } J_{\text{H},1}(i, j) &= (C1_{\text{H}^-}(i, j) - J_{\text{H},2}(i, j) g21_{\text{H}^- \rightarrow \text{H}^-} \\ &\quad - r_1(i, j) C1_{\text{O}^-}(i, j)) / g11_{\text{H}^- \rightarrow \text{H}^-}. \end{aligned} \quad (3)$$

The factors r_1 and r_2 denote the empirically derived ratio of the H^- versus O^- count rates in energy bins 1 and 2 triggered by ISN He. The rationale behind this approach is that ISN He is energetic enough to sputter H^- and O^- atoms off the conversion surface, whereas ISN H of original energies 11–41 eV produces H^- count rates via charge exchange in energy bins 1 and 2 but sputters a negligible amount of H^- or O^- at these energies. The inflight ratios r of the H^- versus O^- count rates are plotted in Figure 5. Similar to the conversion factors of $g3_{\text{He} \rightarrow \text{H}^-}$, these ratios cannot be defined for ISN He energies lower than 70 eV. As a consequence, the H2O2_inflight approach cannot be used either to derive ISN H for a direction with a notable ISN He signal below 70 eV.

The H3_lab approach, with its energy-independent conversion factors, is the only method applicable to all latitudes. However, the retrieved ISN H in the H3_lab maps at latitudes beyond 54° coincide with strong signals of the He Warm Breeze (see Section 4). This interference means that we cannot retrieve any ISN H from the polar regions. No separate energy bin exists there from which ISN He can be derived without the potential contribution of ISN H.

We will treat the H3_inflight method as the default throughout the paper. The differences between the ISN H derived with H3_inflight and H3_lab are small (see beginning of Section 4). The main advantage of the H3_inflight and H3_lab methods compared to H2O2_inflight is that they can be applied to all years whereas H2O2_inflight yields the highest number of pixels with a trustworthy ISN H intensity but can only be applied to 2009–2012 at nominal PAC settings.

The uncertainties of ISN H derived from Equations (2) or (3) are calculated via error propagation as the squared sum of all uncertainties affecting the conversion factors and the measured count rates $C3_{\text{H}^-}(i, j)$, $C2_{\text{H}^-}(i, j)$, and $C1_{\text{H}^-}(i, j)$. The count rate uncertainties are estimated with Equation (1).

The retrieved intensities of ISN H are provided in two different map formats: orbit number versus spin angle and ecliptic longitude versus ecliptic latitude. The first format is the original format of the data acquisition. It is preferable to compare data with model results within the *IBEX* science team as no additional averaging over space or time is applied to the data. The ecliptic format is more general and is preferred for the presentation and discussion of the results in Section 4. That format is produced a posteriori from the orbit versus spin maps by rebinning each pixel of the orbit versus spin map into an equidistant $6^\circ \times 6^\circ$ grid of ecliptic longitude and latitude: we averaged the corresponding ecliptic longitude and latitude of each pair of orbit number and spin angle over the observation times, assumed a field of view of $6.5^\circ \times 6.5^\circ$, and redistributed the ISN H intensity on all (partially) covered ecliptic pixels of the ecliptic map.

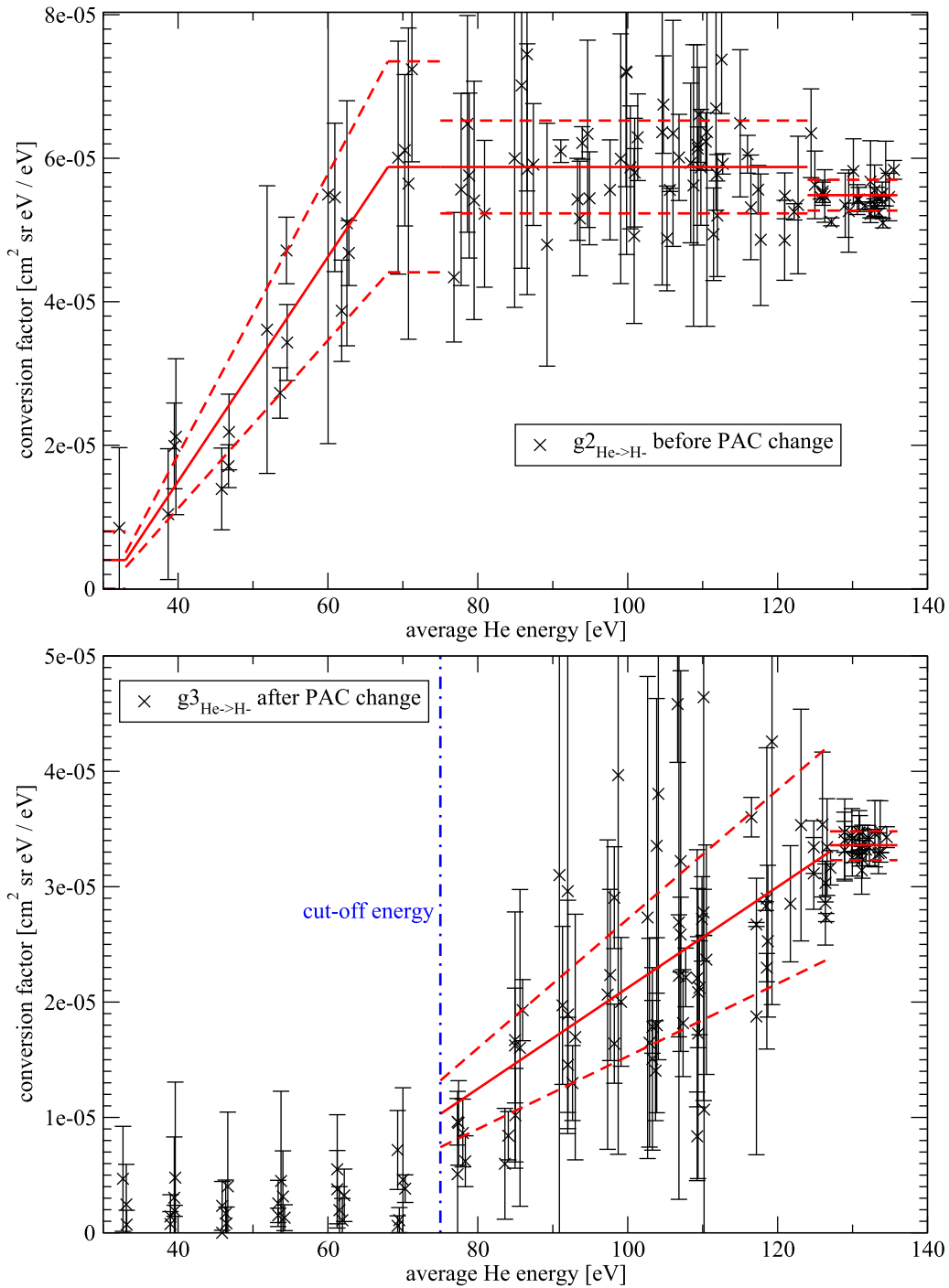


Figure 4. Inflight conversion factors $g^2_{\text{He} \rightarrow \text{H}^-}$ before the PAC change (top) and $g^3_{\text{He} \rightarrow \text{H}^-}$ after the PAC change (bottom) vs. incoming He energy. The conversion factors from all years at the same instrument settings are plotted against He energy derived with the model parameters for the primary and secondary ISN He (Kubiak et al. 2016; Swaczyna et al. 2018). The black symbols are the raw data points, the red solid lines denote the linear fits, and the red dashed lines indicate the 1σ uncertainties of the fits.

3.3. Verification of Conversion Factors for Low-energy Hydrogen Atoms

Throughout this paper, we assume that the conversion factors for neutral hydrogen (impacting the instrument conversion surface at a relative energy of 11–41 eV) to create H^- ions are the ones measured in the laboratory (stated in Table 2). As for the factors describing the He sensitivity, an uncertainty of 30% was always assumed unless stated otherwise (Fuselier et al. 2009). With these conversion factors, we obviously

ignored any possible energy-dependence. A model-independent inflight calibration of the conversion factor $g_{\text{H}^- \rightarrow \text{H}^-}$ would eliminate this uncertainty. Unfortunately, *IBEX-Lo* encounters very few signals of neutral hydrogen with energies between 10 and 40 eV. Adjusting the conversion factors to match the ISN H derived from measurements with model predictions might hide any potential discrepancy between the measured and modeled ISN H signals. Heliospheric hydrogen ENAs, on the other hand, become difficult to discern against the ubiquitous background below 100 eV (Galli et al. 2016). This leaves us

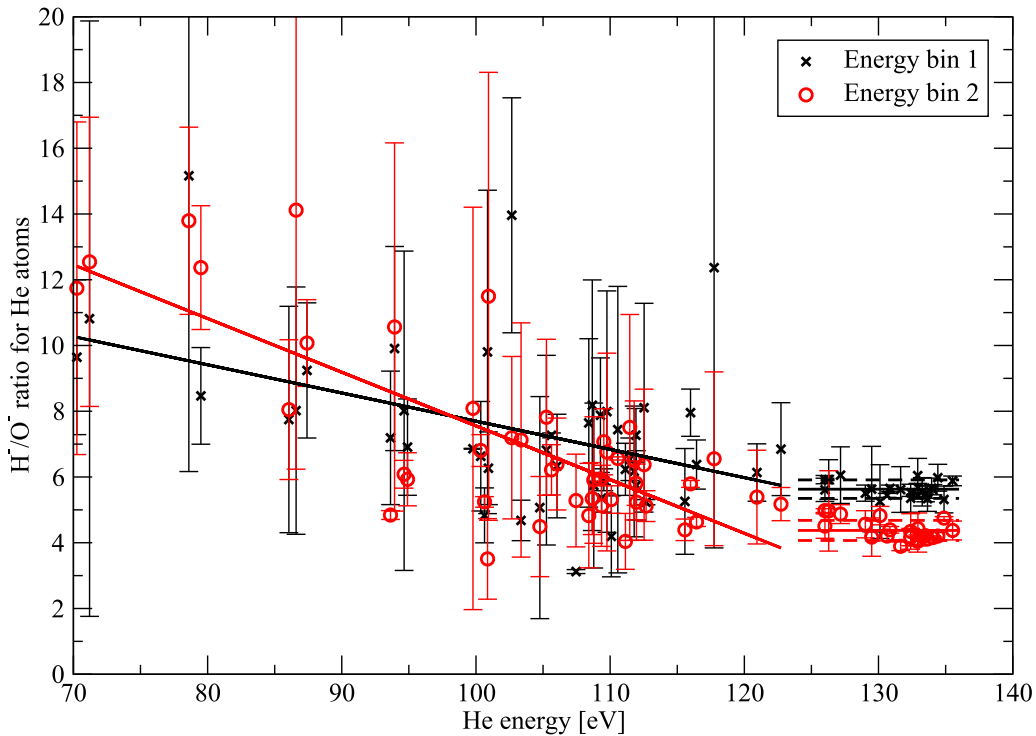


Figure 5. Inflight ratio of H^- count rates vs. O^- count rates triggered by ISN He vs. the modeled He energy for the primary and secondary ISN He from 2009 until 2012. Red circles are the observed ratios in energy bin 2, black symbols denote the ratios in energy bin 1, and solid lines denote linear fits.

only with magnetospheric and lunar ENAs to verify the *IBEX-Lo* response to low-energy hydrogen.

Hydrogen ENAs backscattered from the Moon were observed independently by *IBEX* (McComas et al. 2009b) and by the CENA spectrometer (Barabash et al. 2009) on board the Indian lunar satellite *Chandrayaan-1* in 2009 and thereafter. The CENA and the *IBEX-Lo* instruments were independently calibrated at different facilities (Barabash et al. 2009; Fuselier et al. 2009). For our purpose, the most relevant studies are Rodríguez Moreno et al. (2012), Allegrini et al. (2013), and Futaana et al. (2012). Futaana et al. (2012) described the ENA spectrum observed with CENA in physical units of differential intensity. This spectrum is an average over three orbits on 2009 July 18, when the Moon was in the unperturbed solar wind. We used this spectrum and, assuming the *IBEX-Lo* conversion factors in Table 2, transformed it into a spectrum of H^- count rates per second. If the actual conversion factors for low-energy hydrogen were similar to those from the laboratory calibration, the predicted spectrum should be similar to the spectrum actually observed with *IBEX-Lo*. For the *IBEX-Lo* measurements, we used orbit 58 (2009 December 21) because it has a good signal-to-noise ratio and the Moon was in the solar wind. The ENA energy spectrum measured during orbit 58 is similar to the other orbits studied by Rodríguez Moreno et al. (2012) and Allegrini et al. (2013) when the Moon was in the solar wind. The solar wind parameters looked similar on 2009 July 18 and December 21 (Elliott et al. 2012).

The result of this cross-instrument comparison is shown in Figure 6: red circles denote the predictions based on the CENA spectrum reported by Futaana et al. (2012), and black “x” symbols show the actual *IBEX-Lo* measurements. The agreement of the spectral shapes at energies below 200 eV is excellent between the two different instruments. Around 500 eV, the signal of the lunar ENAs drops rapidly as the

energy approaches the energy of the parent ions, i.e., solar wind protons. The only discrepancy in Figure 6 is the absolute intensity, which differs by a constant factor of 3 for all energies below 200 eV. Because absolute calibration of neutral atom sensors is notoriously challenging, it is not clear which, if any, of the two absolute calibrations is superior. In summary, the physical intensities of the derived ISN H in the following results may be offset by a constant factor, but the relative values of $g_{H^- \rightarrow H^-}$ at the relevant energy bins are confirmed by the cross-comparison for lunar ENAs.

4. Results

We first present the ISN H maps for a year of low solar activity when the ISN H signal can clearly be seen. Figure 7 shows the ISN H between 11 and 21 eV ($J_{H,1}$) in the orbit versus spin angle format for the 2010 season. Subsequently, Figure 8 shows the same results transformed into ecliptic longitude versus latitude. The corresponding maps of intensity between 20–41 eV ($J_{H,2}$) show an order of magnitude less intensity and are dominated by the He Warm Breeze at orbits 55–60. In both energies, the first few orbits of an observation season are also contaminated by magnetospheric signals and should therefore be regarded with caution.

The six panels in Figures 7 and 8 have the following meaning: top-left panel: derived intensity of ISN H in units of $\text{cm}^{-2} \text{sr}^{-1} \text{s}^{-1}$ (approach H3_inflight), top-right panel: corresponding relative uncertainty, red highlights map pixels with an uncertainty larger than the derived intensity value in the left panel. Middle row: same as the first row, but here the energy-independent $g_{\text{He}^- \rightarrow \text{H}^-}$ from the laboratory calibration were assumed (approach H3_lab). Bottom row: analogous to the first row, but here the ISN H was derived from the combination of H^- and O^- count rates in the two lowest energy bins (approach H2O2_inflight).

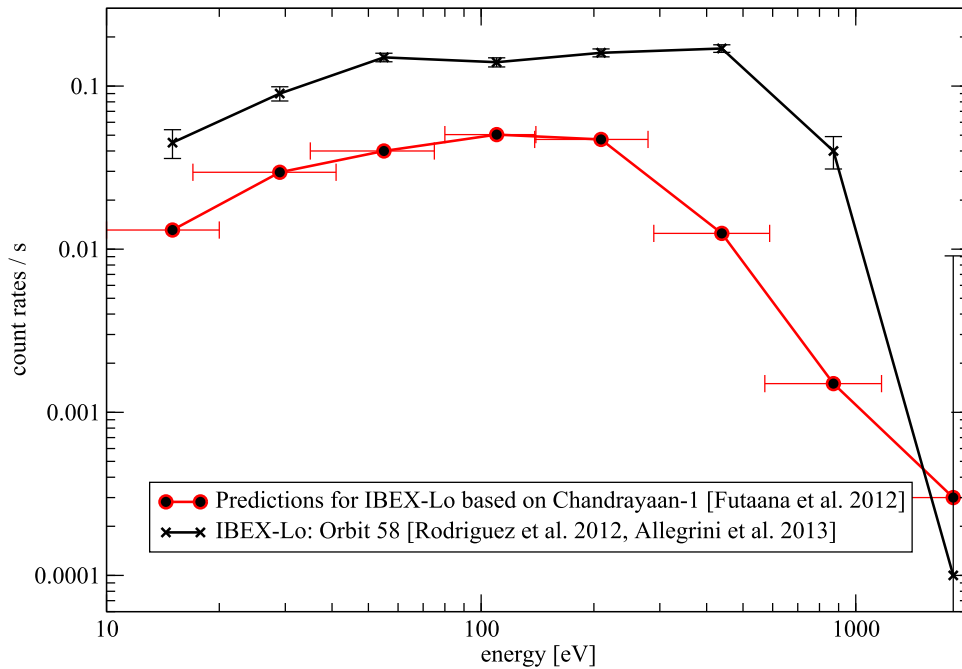


Figure 6. Test of *IBEX-Lo* calibration accuracy with lunar ENAs: predicted count rates from independent measurements with *Chandrayaan-1* (red circles) vs. the actual *IBEX* measurements (black “x” symbols) over the full range of ENAs backscattered from the lunar surface.

In this paper, we concentrate on the process of isolating the ISN H data from *IBEX-Lo* observations. To put the data into context, we resorted to the WTPM code (Sokół et al. 2015) adapted for neutral hydrogen. The ISN H model results of this approach are presented in more detail by Kowalska-Leszczynska et al. (2018b), including a discussion of model assumptions. In short, the WTPM code is based on the paradigm of the classical hot model of the ISN H distribution in the heliosphere (Thomas 1978; Fahr 1979; Wu & Judge 1979) with modifications to account for the dependence of the solar radiation pressure on the solar Ly α emission profile and for the variation of the ionization rate with time and heliolatitude (see Kowalska-Leszczynska et al. 2018a; Sokół et al. 2018 and references therein). The ISN H atoms at 1 au were assumed to be composed of the little-perturbed primary population of interstellar hydrogen and the secondary population, created in the outer heliosheath by charge-exchange interactions between protons from the perturbed plasma flow in the outer heliosheath and the primary interstellar H population. The primary and secondary ISN H populations were modeled as two homogeneous Maxwell–Boltzmann distributions at 150 au from the Sun with the parameters (densities, bulk velocity vectors, and temperatures) based on *Ulysses*, *Voyager*, and previous *IBEX* observations (Bzowski et al. 2015; Kubiak et al. 2016). The numerical values of these ISN H parameters are listed in Table 1 of Kowalska-Leszczynska et al. (2018b). We did not attempt to fit the model parameters to the ISN H data presented here, and we did not include any instrument effects other than collimator filtering.

4.1. Comparison of Retrieval Methods

If different retrieval methods for the same data yield different results, either the method is questionable or the retrieved quantity is poorly constrained from the data. In Section 3, we presented three different retrieval methods (Equations (2) and (3)), adding that we would use the H3_inflight method as default. Here, we motivate our choice. First, we define two

statistical measures to quantify the agreement between two different retrieval methods $m1$, $m0$. If the relative difference in a map pixel is given by

$$d(i, j) = (J_{H,m1}(i, j) - J_{H,m0}(i, j)) / J_{H,m0}(i, j), \quad (4)$$

we define the bias $b = \langle d \rangle$ as the average of the relative deviations over all pixels where both methods yield a significant ISN H signal, and the scatter s as the standard deviation of these relative differences.

The differences of ISN H in the lowest energy bin retrieved with H3_inflight and H3_lab are negligible. The bias is on the order of a few percent, and the scatter between the two similar approaches is 10% or less. This is illustrated for the year 2010 in the top panel of Figure 9: the map shows the relative deviations $d(i, j)$, i.e., zero means perfect agreement between the two approaches (golden pixels in this color scheme). The deviations between H3_inflight and H2O2_lab are larger (bottom panel, same color scheme), but the scatter is typically 20%, smaller than the uncertainty attributed to conversion factors.

We analyzed all years and also the results for the weak $J_{H,2}$ signals in energy bin 2 the same way as we did for Figure 9. We found that the scatter was usually less than 30% except for $J_{H,2}$ during the first four years. We take this as a general caveat about overinterpreting the signals at 20–41 eV. The comprehensive statistics of the differences (Equation (4)) for all years and combinations are given in Tables 3 and 4.

The main argument for using H3_inflight instead of H2O2_inflight as default is that the latter method only works for the first four years of data (see Table 1). We will concentrate on the results derived with the H3_inflight method when discussing the temporal evolution of ISN H (Section 4.2); H2O2_inflight results will be used to examine the spatial distribution of ISN H during the first years (Section 4.3).

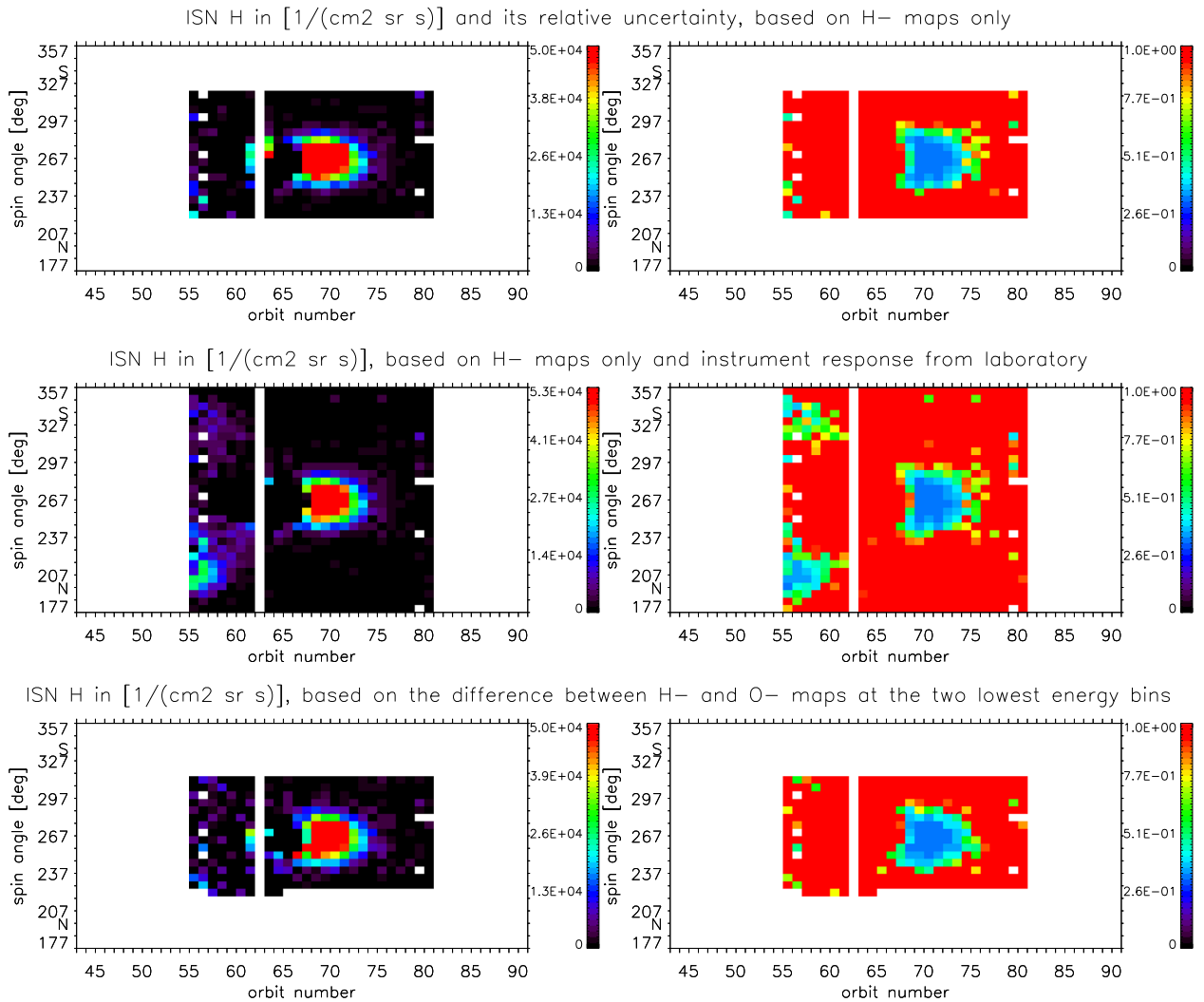


Figure 7. Maps of derived ISN H in $\text{cm}^{-2} \text{sr}^{-1} \text{s}^{-1}$ integrated from 11 to 21 eV (left panels) and their relative uncertainties (right panels) for the year 2010 in orbit number vs. spin angle format. Top panel: H3_inflight method, middle panel: H3_lab method, bottom panel: H2O2_inflight method. The “S” and “N” on the y-axis indicate the orientation in ecliptic latitude, e.g., the bottom row of pixels from spin angles 177° to 183° is centered on the ecliptic north pole.

4.2. The Disappearance and Re-emergence of ISN H with the Solar Cycle

Figures 10 and 11 show the ecliptic maps of ISN H between 11 and 21 eV for all 10 years from 2009–2012 and 2013–2018, derived with the H3_inflight method: the ISN H signal occurs in the ecliptic plane around ecliptic longitudes 260°, roughly 40° or 40 days after the peak of the primary ISN He is recorded with *IBEX* (see top panel of Figure 2). The signal is significant against ISN He and background sources (indicated by relative uncertainties smaller than 1.0 in the right column) at times of low solar activity. The ISN H intensity gradually decreased after 2010 and then dropped to a level below the detection limit around the solar maximum (2014, 2015, and probably 2016). The results for year 2016 are ambiguous because *IBEX*-Lo did not cover most of the relevant viewing directions in the energy steps required to detect ISN H. The first part of this temporal evolution (2009–2012) was already described by Saul et al. (2013) and Schwadron et al. (2013); now we see the signal re-emerge from the background in 2017 as the next solar minimum approaches.

We see in most maps after 2011 a diffuse signal of ISN H coinciding with the primary He signal (around $\lambda_{\text{ecl}} = 225^\circ$)

and with the He Warm Breeze (roughly 170°–200°). The intensity of this ISN H reaches up to $2 \times 10^4 \text{ cm}^{-2} \text{sr}^{-1} \text{s}^{-1}$ both for high (2013–2016) and low solar activities (2017 and 2018). The corresponding uncertainties in the right column (red pixels with relative uncertainties ≥ 1) indicate that these ISN H intensities are not significant compared to the ISN He signal, which is orders of magnitude more intense at ecliptic longitudes 170°–240°. Moreover, the results of the H3_lab approach markedly differ for these regions from the H3_inflight results in Figures 10 and 11. For all these reasons, the apparent ISN H intensities at 170°–240° with relative uncertainties larger than unity should be interpreted as upper limits of any potential ISN H hiding in the ISN He signal.

From the global maps of ISN H in Figures 10 and 11, we derived time series of ISN H: Figure 12 shows the intensity of ISN H (in $\text{cm}^{-2} \text{sr}^{-1} \text{s}^{-1}$) in energy bin 1 (red “x” symbols) and bin 2 (blue circles) versus year of observation at the map pixel of highest ISN H intensity ($\lambda_{\text{ecl}} = 261^\circ$, $\beta_{\text{ecl}} = 3^\circ$). The magenta triangles show the ISN H intensity predicted with the WTPM for this viewing direction. Figure 13 shows the total flux F of ISN H versus years in units of $\text{cm}^{-2} \text{s}^{-1}$. The flux is the sum of the intensity, times 0.011 sr (corresponding to a $6^\circ \times 6^\circ$ pixel), from all pixels within $|\beta_{\text{ecl}}| \leq 30^\circ$ and

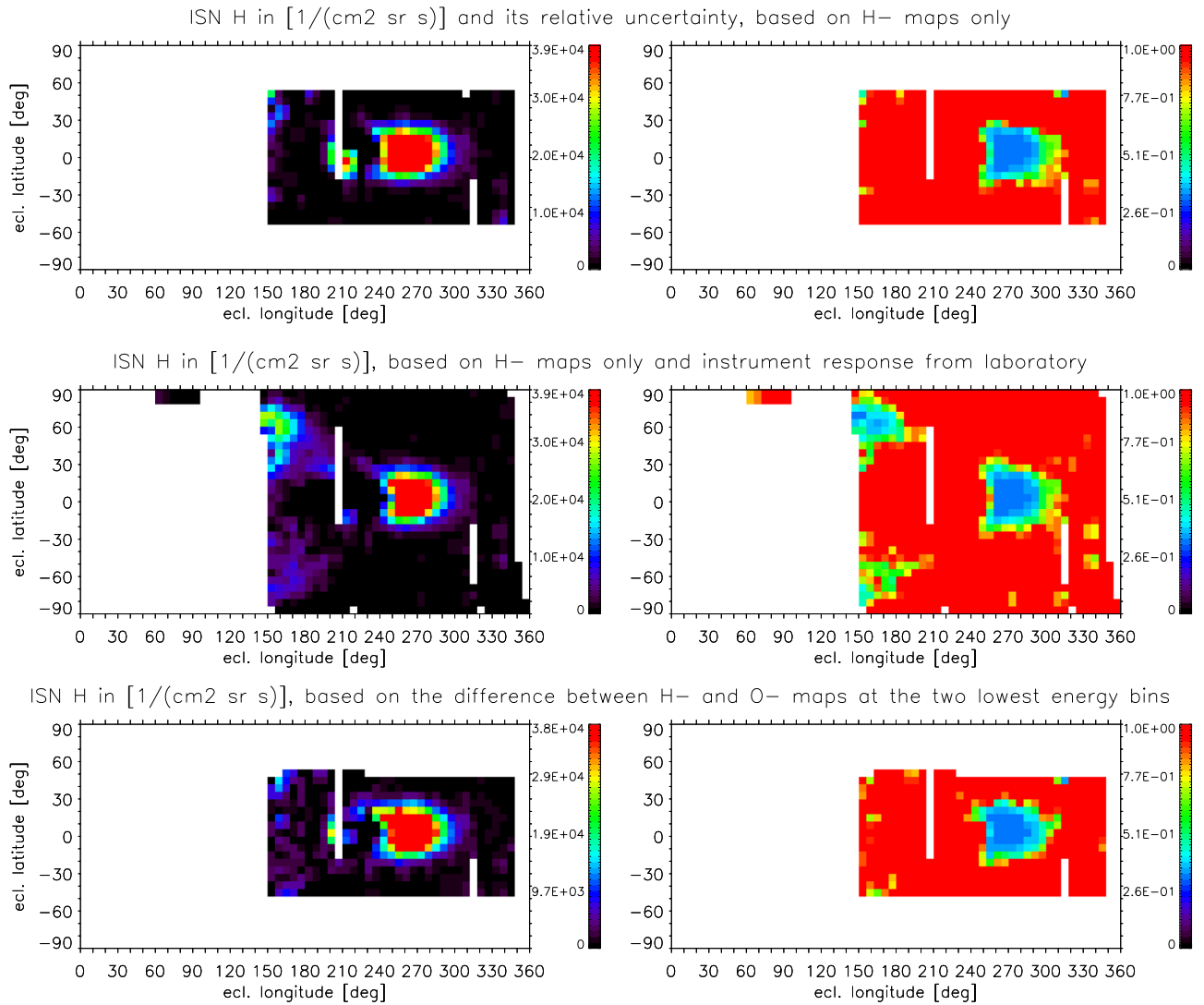


Figure 8. The same data for the derived ISN H for 2010 as in Figure 7, but the maps have been transformed into ecliptic coordinates.

$180^\circ \leq \lambda_{\text{ecl}} \leq 330^\circ$ where a distinct ISN H signal with a relative uncertainty < 1 appeared both at 11–21 eV and 20–41 eV. The error bars ascribed to the total flux are the square sum of the statistical errors plus the systematic calibration uncertainty of 30%.

4.2.1. Interpretation of Temporal Evolution

Whereas the temporal evolution of the model and observations in Figure 12 agree qualitatively, the changes observed in the lowest energy bin are more extreme than expected. These differences can have several reasons: the assumed densities, inflow velocities, and temperatures of the two ISN H populations in the WTPM model were not yet optimized against available observations, and the solar radiation pressure might be biased (see discussion in Kowalska-Leszczynska et al. 2018b). Moreover, WTPM calculates the total intensity of the ISN H in the *IBEX* reference frame after passing through the *IBEX-Lo* collimator. Energy-dependent detection efficiencies and the split of counts into different energy bins are not included in this model version. This is relevant because the typical energy of the modeled ISN H (the weighted mean of the peak energy of the primary and secondary ISN H populations)

changes from 22 to 16 eV and back to 23 eV for the time series from 2009 to 2018 in Figure 13. Although a decrease of instrument sensitivity with incoming H energy is expected, it seems unlikely that the order of magnitude change, observed in the lowest energy bin for 2015 versus 2009 or 2018, is attributable to a poorly known instrument response alone. The count rates in the lowest energy bin caused by neutral H beams of 15 and 29 eV differed only by a ratio of 4.23 divided by 7.29 during calibration, respectively (see Table 2).

The high-energy ISN H in the energy bin from 20 to 41 eV (blue symbols in Figure 12) depends critically on energy: $J_{\text{H},2}$ exceeds the background significantly only in those years for which the model predicts an average H energy above 21 eV (2009, 2010, 2017, and 2018). But also for these years, the low-energy ISN H signal is much larger. Figures 12 and 13 show that for both the peak position and the integrated flux the low-energy ISN H is more abundant by an order of magnitude for all years of low solar activity. More precisely, the ratios of fluxes $F_{\text{H},1}/F_{\text{H},2}$ in Figure 13 are 16.8, 18.0, 16.2, 4.0, 5.3, 2.1, 2.3, 7.1, and 7.7 for the years from 2009 to 2018 without 2016. This discrepancy between the modeled energy and the energy inferred from observations was already pointed out by Katushkina et al. (2015). The actual energy of ISN H might

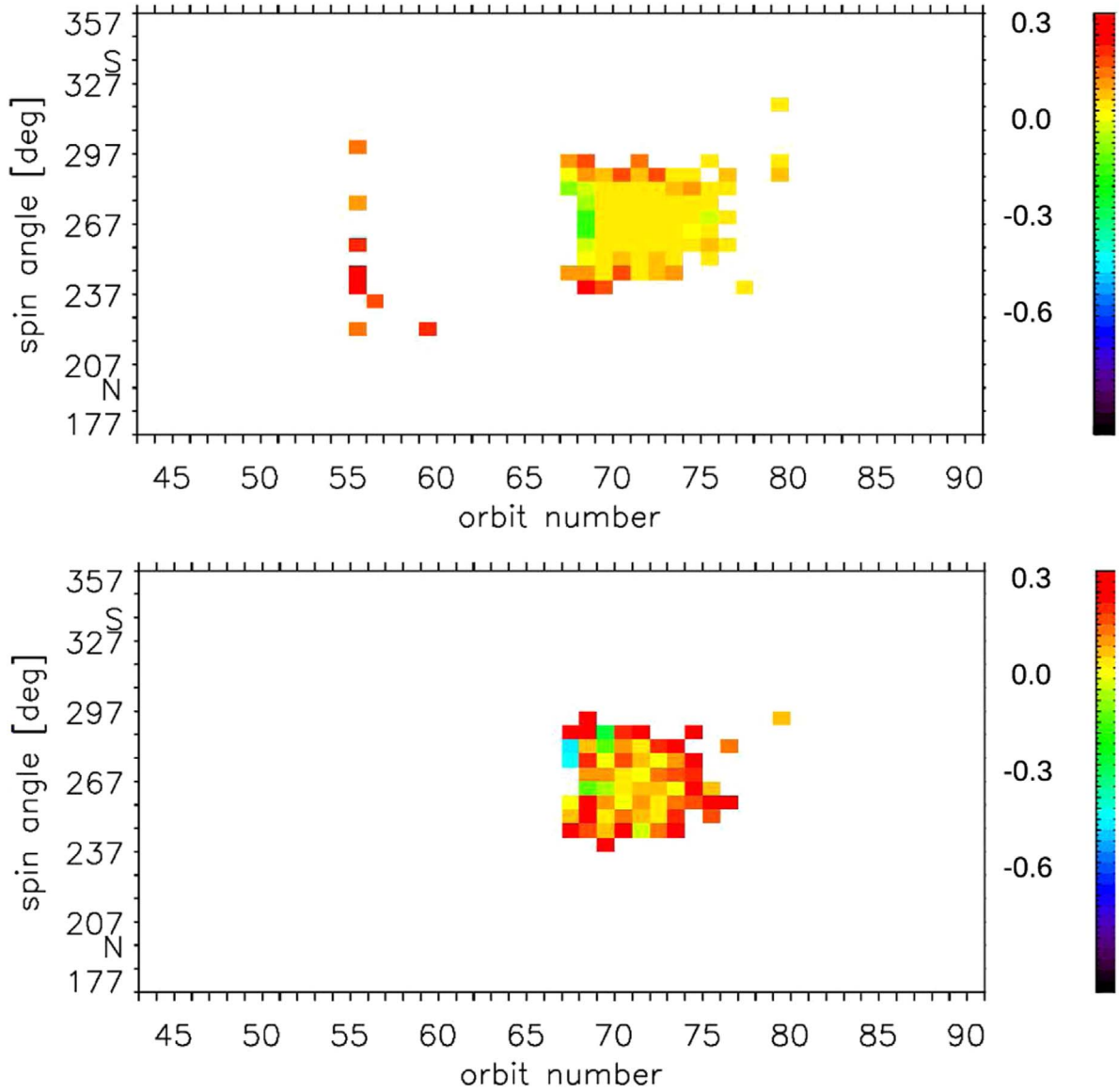


Figure 9. Relative differences between the retrieved ISN H at energies 11–21 eV derived with method H3_lab vs. method H3_inflight (top) and H2O2_inflight vs. H3_inflight (bottom) for the year 2010. Golden pixels with value 0 mean perfect agreement between different retrieval methods. The “S” and “N” on the y-axis indicate the orientation in ecliptic latitude, e.g., the bottom row of pixels from spin angles 177° to 183° is centered on the ecliptic north pole.

Table 3
Cross-comparison of the Three Different ISN H Retrieval Methods for 2009–2012 (before PAC Change)

Comparison	2009	2010	2011	2012
ISN H1, H3_lab versus H3_inflight	$b = 0.04$ $s = 0.11$	$b = 0.02$ $s = 0.08$	$b = 0.01$ $s = 0.07$	$b = 0.02$ $s = 0.09$
ISN H1, H2O2_inflight versus H3_inflight	$b = 0.09$ $s = 0.21$	$b = 0.09$ $s = 0.21$	$b = 0.10$ $s = 0.21$	$b = 0.26$ $s = 0.22$
ISN H2, H3_lab versus H3_inflight	$b = 0.15$ $s = 0.28$	$b = 0.19$ $s = 0.32$	$b = 0.33$ $s = 0.41$	$b = 0.18$ $s = 0.27$
ISN H2, H2O2_inflight versus H3_inflight	$b = 0.38$ $s = 0.47$	$b = 0.41$ $s = 0.46$	$b = 0.15$ $s = 0.21$	$b = 0.12$ $s = 0.27$

Note. The bias b denotes the average of the relative pixel-by-pixel differences between two methods, and the scatter s denotes the standard deviation thereof.

be lower than predicted, and/or H atoms of $\simeq 20$ eV might lose a larger fraction of their energy in *IBEX*-Lo than the 15% expected from the laboratory calibration between 100 eV and 1 keV (Fuselier et al. 2009). The decrease of the $F_{H,1}/F_{H,2}$ ratio from low to high solar activity might be an artifact, as the intensities in both energy bins become indistinguishable against the background in most map pixels. The factor of 2 difference in flux and peak intensity of ISN H between 2009 and 2018 warrants closer investigation after the approaching solar minimum.

4.3. Profiles of ISN H with Longitude and Latitude

This section is dedicated to the spatial distribution of ISN H for a given year. Like the intensities, the ecliptic longitude where the observed ISN H intensity peaks is expected to vary with solar activity from 2009 to 2018. However, the

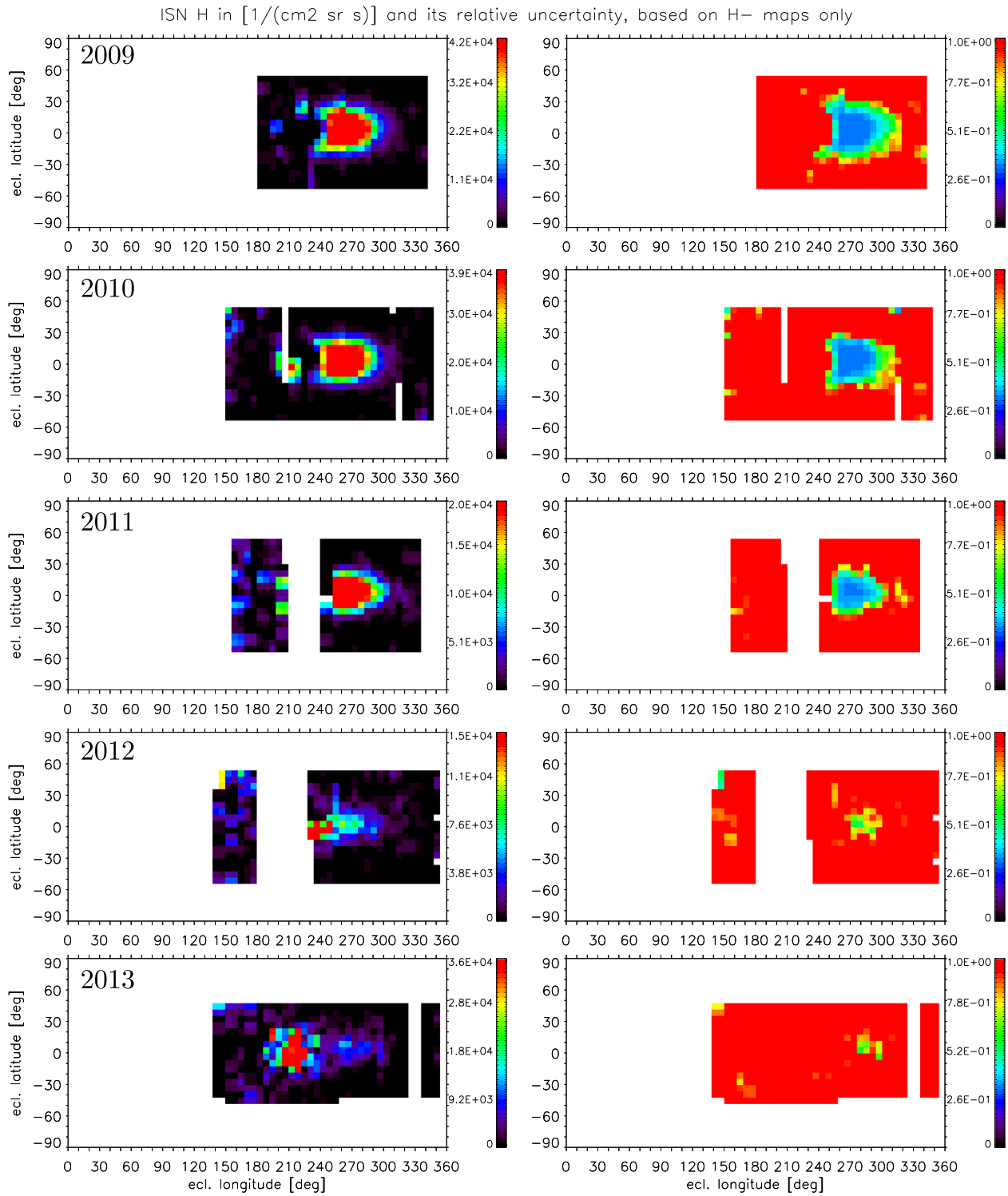


Figure 10. Maps of the derived ISN H in $\text{cm}^{-2} \text{sr}^{-1} \text{s}^{-1}$ integrated from 11 to 21 eV (left panels) and their relative uncertainties (right panels) in ecliptic coordinates for the years 2009–2013 (top to bottom); H3_inflight approach.

Table 4

Cross-comparison of the H3_inflight and H3_lab Retrieval Approach for 2013–2018 (after PAC change), in the Same Format as Table 3

Comparison	2013	2014	2015	2016	2017	2018
ISN H1, H3_lab versus H3_inflight	$b = -0.04$ $s = 0.09$	$b = -0.03$ $s = 0.09$	$b = 0.01$ $s = 0.12$	$b = 0.02$ $s = 0.09$	$b = -0.06$ $s = 0.08$	$b = -0.04$ $s = 0.07$
ISN H2, H3_lab versus H3_inflight	$b = 0.09$ $s = 0.17$	$b = 0.07$ $s = 0.14$	$b = 0.05$ $s = 0.13$	$b = 0.06$ $s = 0.10$	$b = 0.04$ $s = 0.15$	$b = 0.10$ $s = 0.17$

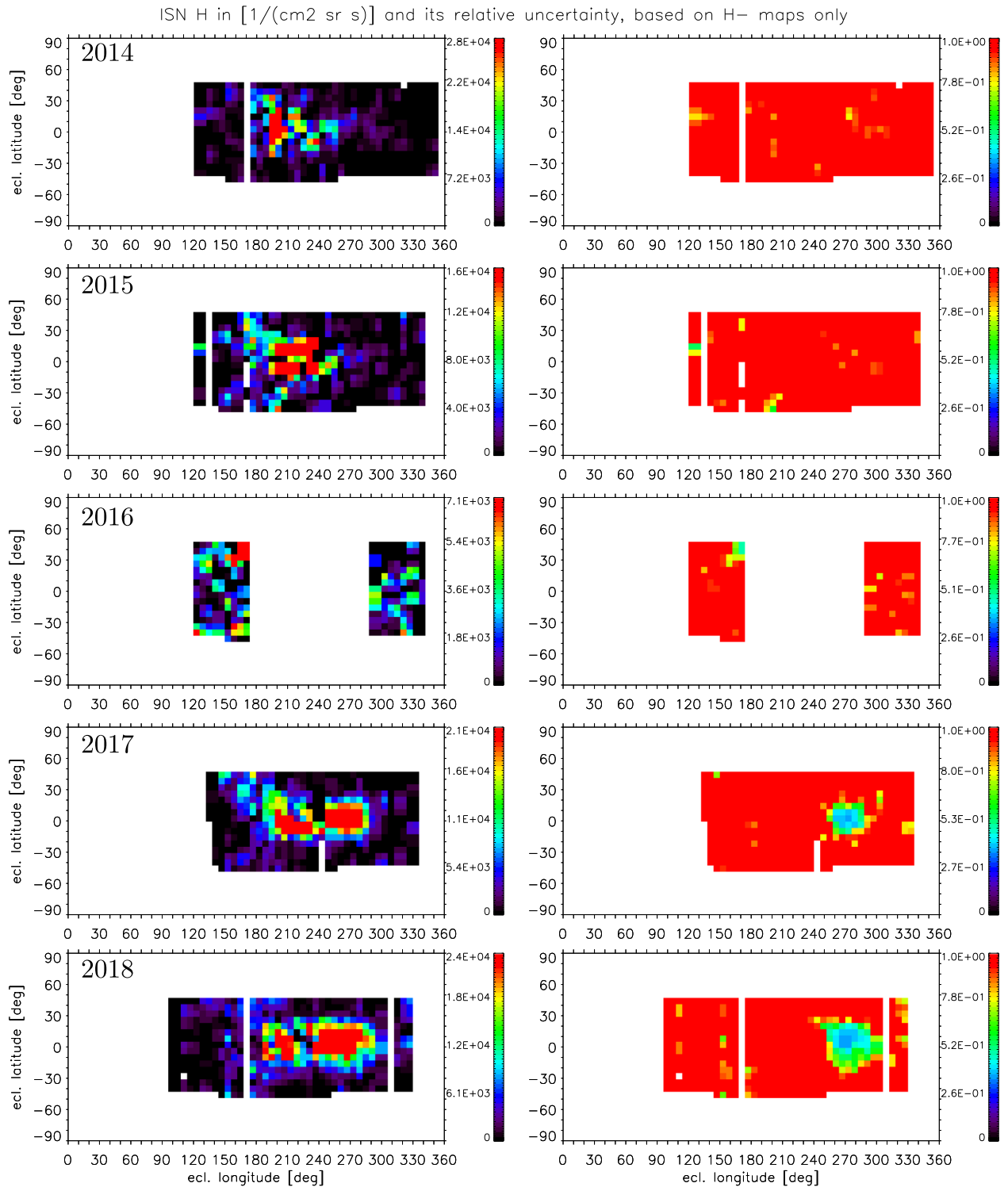


Figure 11. Maps of the derived ISN H in $\text{cm}^{-2} \text{sr}^{-1} \text{s}^{-1}$ integrated from 11 to 21 eV (left panels) and their relative uncertainties (right panels) in ecliptic coordinates for the years 2014–2018 (top to bottom); H3_inflight approach.

ecliptic longitude of the maximum ISN H intensity cannot be constrained in any year against earlier orbits with the H3_inflight or H3_lab approaches (even if the 30% uncertainty in $g_{\text{H}^- \rightarrow \text{H}}$ is ignored) because ISN He is orders of magnitude more intense than ISN H. The upper limit of the peak longitude in the ecliptic plane is $\lambda_{\text{ecl}} = 270^\circ$ for all years when the ISN H signal is discernible against the background (2009–2014, 2017, and 2018). The H2O2_inflight approach results in smaller error

bars; here, the signal can be constrained to $261^\circ \pm 9^\circ$ for 2010. In this section, we therefore rely on the H2O2_inflight results.

Figure 14 shows the longitudinal cross-section of ISN H intensities in the lowest energy bin for the years 2009–2012. Since we are interested only in the relative change of ISN H intensity within the same year and energy, we omitted the 30% calibration uncertainty for this plot. In all years, the ISN H signal at 11–21 eV in the ecliptic ($\pm 30^\circ$ ecliptic latitudes)

Peak intensity of ISN H

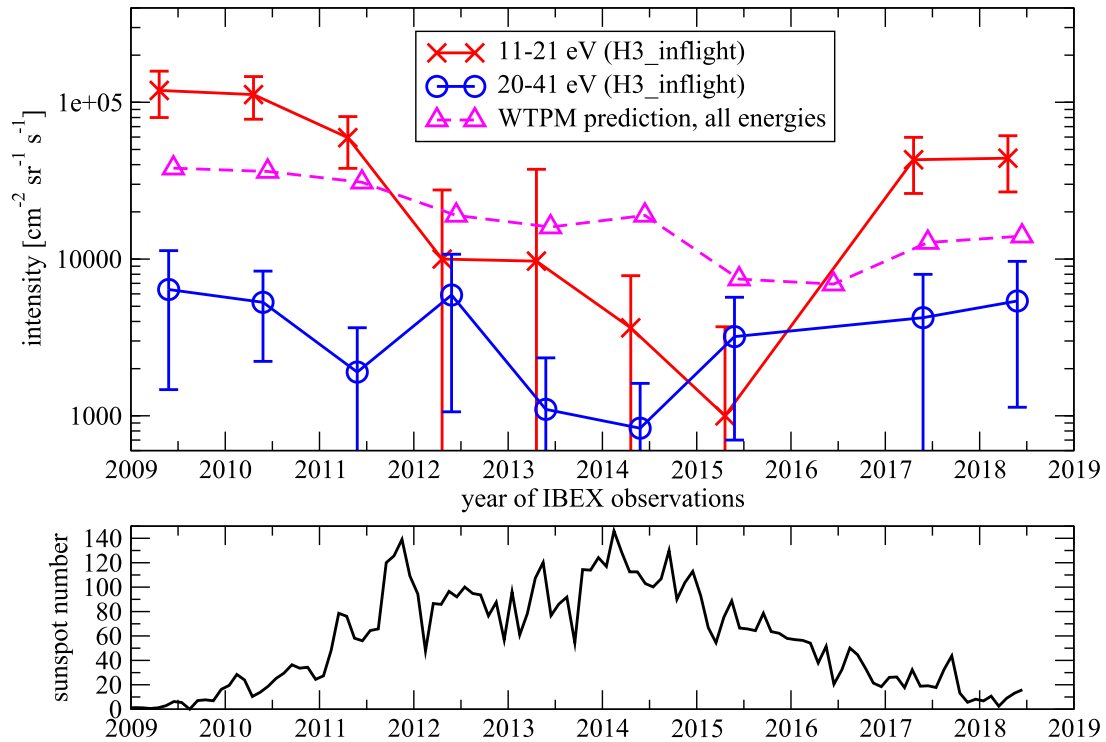


Figure 12. Time series of maximum ISN H intensity (top) and solar activity (bottom). The top panel shows the peak intensity of ISN H in $\text{cm}^{-2} \text{sr}^{-1} \text{s}^{-1}$ between 11 and 21 eV (red line) and between 20 and 41 eV (blue line) observed in the ecliptic plane vs. year of observation. The data points of 2016 had to be skipped because only a fraction of the potential ISN H signal was covered. The magenta triangles show the intensity of ISN H for the same viewing direction predicted with the WTPM code. The bottom panel shows the sunspot number as a proxy for solar activity (SILSO, World Data Center 2008).

Total flux of ISN H

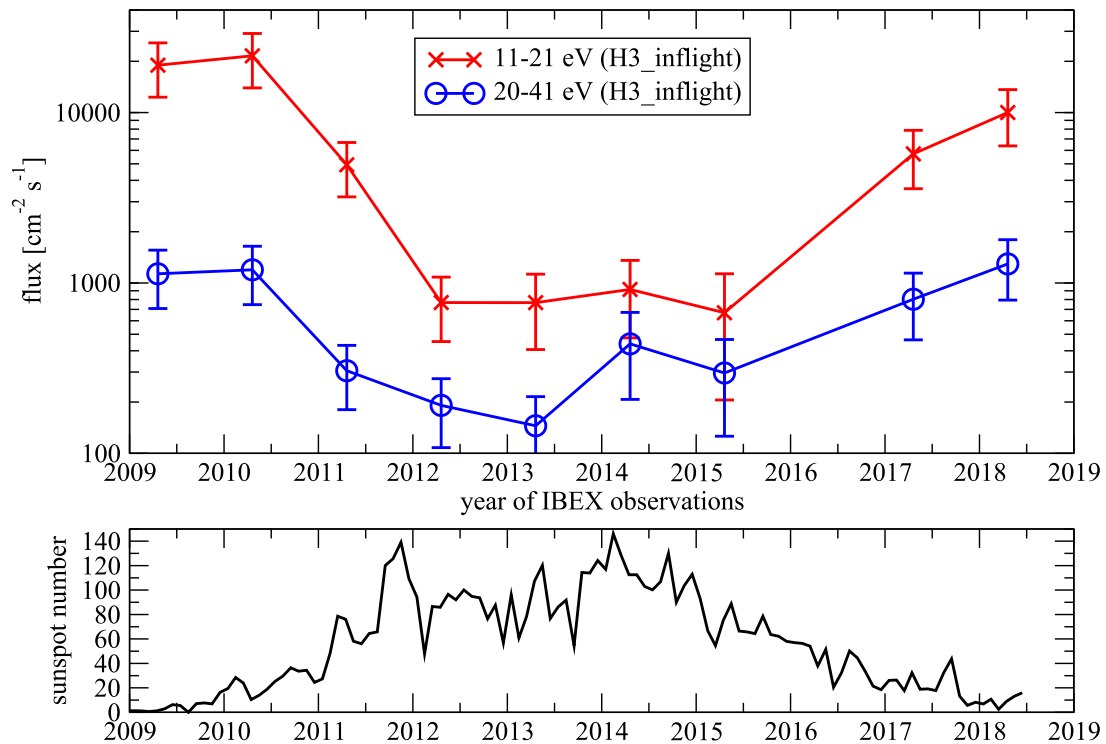


Figure 13. Time series of ISN H flux (top) and solar activity (bottom). The top panel shows the total flux of ISN H in $\text{cm}^{-2} \text{s}^{-1}$ between 11 and 21 eV (red line) and between 20 and 41 eV (blue line) vs. year of observation. The data points of 2016 had to be skipped because only a fraction of the potential ISN H signal was covered. The bottom panel shows the sunspot number as a proxy for solar activity (SILSO, World Data Center 2008).

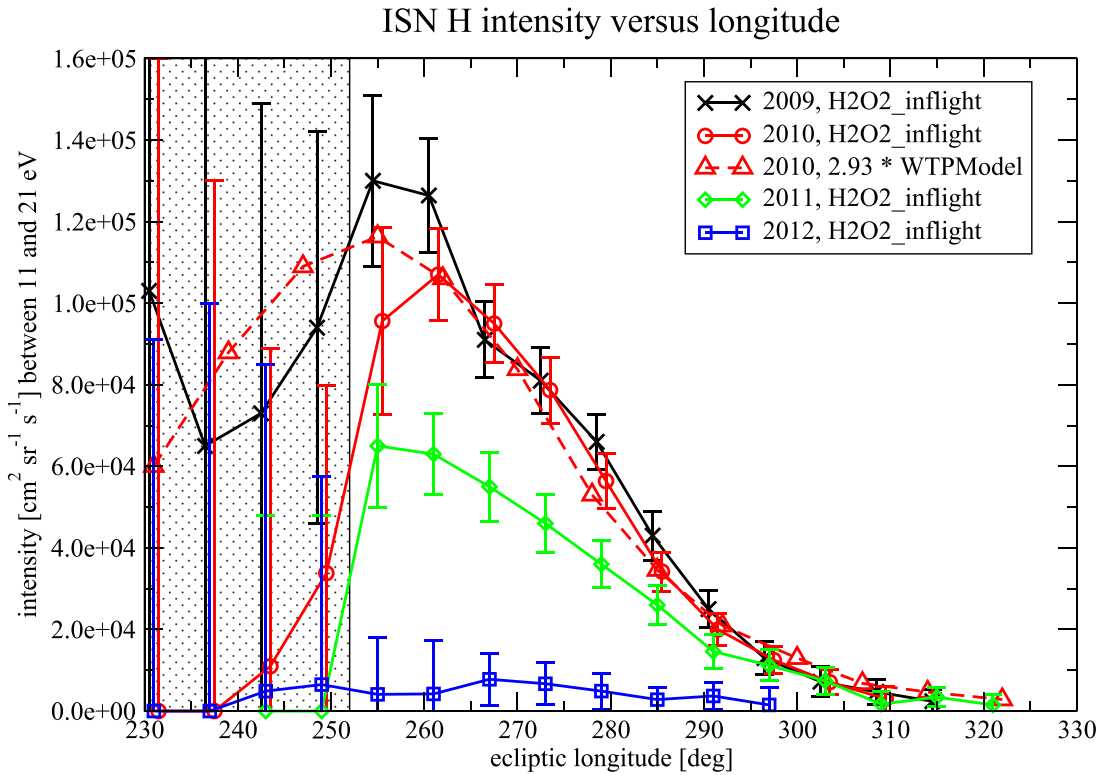


Figure 14. Longitudinal profile of ISN H intensity in $\text{cm}^{-2} \text{sr}^{-1} \text{s}^{-1}$ at $\beta_{\text{ecl}} = 0^\circ \dots 6^\circ$ between 11 and 21 eV, derived with the H2O2_inflight approach for the first four years of *IBEX* observations. The ISN H signal is reduced almost to background level because of the increasing solar activity. The red triangles show the model predictions for the integrated ISN H intensity in 2010, multiplied by an empirically derived constant of 2.93. The large uncertainties of the derived ISN H at $\lambda_{\text{ecl}} < 254^\circ$ are a consequence of the intense ISN He signal there (shaded region).

reaches ecliptic longitudes of $312^\circ \pm 12^\circ$ before blending into the background with upper limits of a few $1000 \text{ cm}^{-2} \text{sr}^{-1} \text{s}^{-1}$. In 2009, 2010, 2017, and 2018, the ISN H at 20–41 eV appears to peak at the same longitude as that for 11–21 eV. However, that longitude again is ill constrained because of the strong ISN He signal (shaded region in Figure 14). The longitudinal profile of ISN H derived at 20–41 eV, scaled by a constant factor, does not significantly differ from the low-energy profiles shown in Figure 14. For the year 2010, we added the modeled ISN H intensity, multiplied by an empirically derived constant of 2.93 (red triangles). The shape of ISN H in the longitudinal direction agrees between the model and observations: the modeled intensities are within the 1σ uncertainties of observations at 12 of the 14 different longitudes between 230° and 310° ecliptic longitude. The average H energy predicted by the model varies only between 19 and 22 eV along this range. A similar agreement is found for the year 2009.

We also compiled the latitudinal profile of the retrieved ISN H (H2O2_inflight approach) in 11–21 eV at 261° ecliptic longitude for the years 2009–2012 (Figure 15). The ISN H decrease toward higher solar activity is evident again. Most observations are well constrained in both directions of the peak because no strong ISN He signal complicates interpretation in the latitudinal direction. Such latitudinal profiles are therefore well suited for future analysis and more detailed comparisons with model predictions.

4.3.1. Interpretation of Spatial Distribution

Although such comparisons are not the main focus of this paper, one systematic discrepancy between observations and model must be noted: the predicted ISN H falls off more slowly

at off-ecliptic latitudes than is actually observed. The red triangles in Figure 15 show again the case of 2010, but a similar picture emerges for 2009. The observed latitudinal distribution of ISN H at higher energies (20–41 eV) falls off even more rapidly. Here, only the intensities at $\beta_{\text{ecl}} = -3^\circ, 3^\circ$, and 9° significantly exceed background levels. The model predicts average H energies of 20.1, 21.0, 21.6, 21.7, 21.4, 20.7, and 19.7 eV for $\beta_{\text{ecl}} = -15^\circ$ to 21° . This reflects the bandwidth of energy bin 2, which was found to extend to roughly 20 eV during laboratory calibration with neutral H. The range of modeled H energies for the different latitudes indicates that a wrong assumption about the sensitivity of *IBEX*-Lo for low-energy H cannot fully explain the discrepancy in latitudinal distribution (Figure 15). The discrepancy between data and model becomes evident already at $\beta_{\text{ecl}} = \pm 15^\circ$ where the average H energy is 20 ± 1 eV, i.e., the same as for the longitudinal distributions where the observed and modeled profiles agree (Figure 14).

5. Conclusions

We have compiled model-free maps of all *IBEX* observations of ISN H available so far from 2009 to 2018. These maps will serve as a starting point for future comparison with model predictions, thus improving models of the ISN inflow, radiation pressure, and loss processes affecting neutral hydrogen inside the heliosphere.

The disappearance and re-emergence of ISN H with changing solar activity agrees with expectations. There is no time lag between the solar activity level and the measured intensity of ISN H at 1 au. The basic concept of ISN H trajectories dominated by radiation forces and loss processes

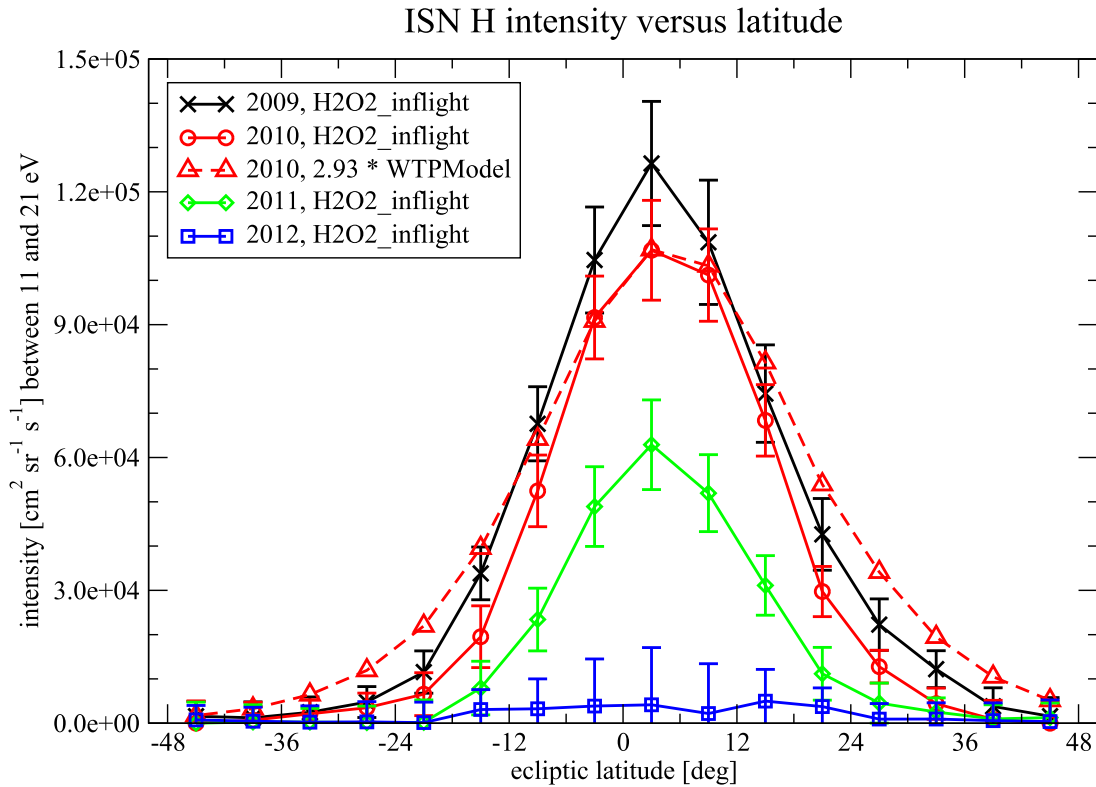


Figure 15. Latitudinal profile of the ISN H intensity in $\text{cm}^{-2} \text{sr}^{-1} \text{s}^{-1}$ at $\lambda_{\text{ecl}} = 258^\circ \dots 264^\circ$ between 11 and 21 eV, derived with the H2O2_inflight approach for the first four years of *IBEX* observations. The red triangles show the model predictions for the integrated ISN H intensity in 2010, multiplied by an empirically derived constant of 2.93.

close to the Sun therefore is correct. The expected shift of the ISN H peak longitude with increasing solar activity could not be identified unambiguously in this analysis, possibly due to the limited spatial resolution and low intensities during years of high solar activity. The evolution of the ISN H peak position with solar activity will be the topic of future studies. Independent of spatial resolution, the ISN H derived in earlier orbits (ecliptic longitudes smaller than 260°) usually is ill constrained because of the intense ISN He signal there. For quantitative comparison to models, latitudinal profiles with their much smaller error bars may be a better test case. The ISN H derived at higher energies 20–41 eV can only be determined against the background for a few map pixels for the years close to solar minimum (2009, 2010, 2017, and 2018). Its use for comparison to a global ISN model may therefore be questionable. We confirm previous observations of the strong depletion of ISN H in energy bin 2 compared to the lowest energy bin (Saul et al. 2012, 2013; Schwadron et al. 2013). No ISN H is detected in energy bin 2 whenever the modeled average H energy drops below 21 eV.




Our preliminary analysis shows that the qualitative evolution of ISN H over the solar cycle and the intensity distribution in the ecliptic plane agree between the observations and the WTPM code. On the other hand, the ISN H intensity measured at 11–21 eV reacts much more sensitively to the solar cycle, and outside the ecliptic plane, the observed signal drops off more rapidly than predicted by the model. The solar radiation pressure and loss processes affecting ISN H close to the Sun assumed in the WTPM may have to be updated. In their recent reassessment, Kowalska-Leszczynska et al. (2018b) also concluded that radiation pressure effects on ISN H in the

heliosphere are “not understood as well as it has been thought.” We must keep in mind, however, that the preliminary model results presented here did not take into account the energy-dependence of the instrument sensitivity nor the finite range of the energy bins. As next steps, we therefore will model the *IBEX*-Lo count rates more precisely by taking into account the full energy distribution of ISN H and variations of the instrument sensitivity with H energy. Moreover, we will compare the results of two updated ISN models with each other.

We thank all of the outstanding men and women who have made the *IBEX* mission such a wonderful success. This work was carried out as part of the *IBEX* project, with support from NASA’s Explorer Program. A.G. and P.W. thank the Swiss National Science foundation for financial support. E.M. is grateful for support from ISSI for an extended visit in Bern during the formative stage of this study. Research at SwRI was funded by a subcontract from Princeton University. M.B., M.A.K., I.K.-L., and J.M.S. were supported by Polish NCN grant 2018/M/ST9/00036.

ORCID iDs

A. Galli <https://orcid.org/0000-0003-2425-3793>
P. Wurz <https://orcid.org/0000-0002-2603-1169>
F. Rahmanifard <https://orcid.org/0000-0001-9316-0553>
N. A. Schwadron <https://orcid.org/0000-0002-3737-9283>
M. Bzowski <https://orcid.org/0000-0003-3957-2359>
I. Kowalska-Leszczynska <https://orcid.org/0000-0002-6569-3800>

J. M. Sokół  <https://orcid.org/0000-0002-4173-3601>
 P. Swaczyna  <https://orcid.org/0000-0002-9033-0809>
 D. J. McComas  <https://orcid.org/0000-0001-6160-1158>

References

- Allegrini, F., Dayeh, M. A., Desai, M. I., et al. 2013, *P&SS*, **85**, 232
 Barabash, S., Bhardwaj, A., Wieser, M., et al. 2009, *CSci*, **96**, 526
 Bzowski, M., Kubiak, M. A., Czechowski, A., & Grygorczuk, J. 2017, *ApJ*, **845**, 15
 Bzowski, M., Swaczyna, P., Kubiak, M. A., et al. 2015, *ApJS*, **220**, 28
 Elliott, H. A., Henney, C. J., McComas, D. J., Smith, C. W., & Vasquez, B. J. 2012, *JGR*, **117**, A09102
 Fahr, H. J. 1979, *A&A*, **77**, 101
 Funsten, H. O., Allegrini, F., Bochsler, P., et al. 2009, *SSRv*, **146**, 75
 Fuselier, S. A., Bochsler, P., Chornay, D., et al. 2009, *SSRv*, **146**, 117
 Futaana, Y., Barabash, S., Wieser, M., et al. 2012, *JGR*, **117**, E05005
 Galli, A., Wurz, P., Park, J., et al. 2015, *ApJ*, **220**, 30
 Galli, A., Wurz, P., Schwadron, N. A., et al. 2016, *ApJ*, **821**, 107
 Galli, A., Wurz, P., Schwadron, N. A., et al. 2017, *ApJ*, **851**, 2
 Gloeckler, G., & Geiss, J. 2001, in *AIP Conf. Proc.* 598, *Solar and Galactic Composition: A Joint SOHO-ACE Workshop*, ed. R. F. Wimmer-Schweingruber (Meville, NY: AIP), 281
 Katushkina, O. A., Izmodenov, V. V., Alexashov, D. B., Schwadron, N. A., & McComas, D. J. 2015, *ApJS*, **220**, 33
 Kowalska-Leszczynska, I., Bzowski, M., Sokół, J. M., & Kubiak, M. A. 2018a, *ApJ*, **852**, 115
 Kowalska-Leszczynska, I., Bzowski, M., Sokół, J. M., & Kubiak, M. A. 2018b, *ApJ*, **868**, 49
 Kubiak, M. A., Bzowski, M., Sokół, J. M., et al. 2014, *ApJS*, **213**, 29
 Kubiak, M. A., Swaczyna, P., Bzowski, M., et al. 2016, *ApJS*, **223**, 25
 McComas, D. J., Allegrini, F., Bochsler, P., et al. 2009a, *SSRv*, **146**, 11
 McComas, D. J., Allegrini, F., Bochsler, P., et al. 2009b, *GeoRL*, **36**, L12104
 Möbius, E., Bochsler, P., Bzowski, M., et al. 2012, *ApJS*, **198**, 11
 Möbius, E., Fuselier, S., Granoff, M., et al. 2008, in *Proc. of the 30th Int. Cosmic Ray Conf.* 1, ed. R. Caballero et al. (Universidad Nacional Autonoma de Mexico), 841
 Müller, H.-R., & Zank, G. P. 2004, *JGR*, **109**, A07104
 Park, J., Kucharek, H., Möbius, E., et al. 2016, *ApJ*, **833**, 130
 Rodríguez Moreno, D. F., Saul, L., Wurz, P., et al. 2012, *P&SS*, **60**, 297
 Saul, L., Bzowski, M., Fuselier, S. A., et al. 2013, *ApJ*, **767**, 130
 Saul, L., Wurz, P., Rodríguez, D., et al. 2012, *ApJS*, **198**, 14
 Schwadron, N. A., Möbius, E., Kucharek, H., et al. 2013, *ApJ*, **775**, 86
 SILSO, World Data Center 2008, Sunspot Number and Long-term Solar Observations, Royal Observatory of Belgium 2008–2014, International Sunspot Number Monthly Bulletin and Online Catalogue, <http://www.sidc.be/silso>
 Sokół, J. M., Bzowski, M., & Tokumaru, M. 2018, *ApJ*, submitted (arXiv:1809.09823)
 Sokół, J. M., Bzowski, M., Tokumaru, M., Fujiki, K., & McComas, D. J. 2013, *SoPh*, **285**, 167
 Sokół, J. M., Kubiak, M. A., Bzowski, M., & Swaczyna, P. 2015, *ApJS*, **220**, 27
 Swaczyna, P., Bzowski, M., Kubiak, M. A., et al. 2018, *ApJ*, **854**, 2
 Thomas, G. E. 1978, *AREPS*, **6**, 173
 Wu, F. M., & Judge, D. L. 1979, *ApJ*, **231**, 594
 Wurz, P., Saul, L., Scheer, J. A., et al. 2008, *JAP*, **103**, 054905
 Zirnstein, E. J., Kumar, R., Heerikhuisen, J., McComas, D. J., & Galli, A. 2018, *ApJ*, **860**, 170